

# Correction of Physiologically Induced Global Off-Resonance Effects in Dynamic Echo-Planar and Spiral Functional Imaging

Josef Pfeuffer,<sup>1\*</sup> Pierre-Francois Van de Moortele,<sup>1</sup> Kamil Ugurbil,<sup>1</sup> Xiaoping Hu,<sup>1</sup> and Gary H. Glover<sup>2</sup>

**In functional magnetic resonance imaging, a rapid method such as echo-planar (EPI) or spiral is used to collect a dynamic series of images. These techniques are sensitive to changes in resonance frequency which can arise from respiration and are more significant at high magnetic fields. To decrease the noise from respiration-induced phase and frequency fluctuations, a simple correction of the “dynamic off-resonance in *k*-space” (DORK) was developed. The correction uses phase information from the center of *k*-space and a navigator echo and is illustrated with dynamic scans of single-shot and segmented EPI and, for the first time, spiral imaging of the human brain at 7 T. Image noise in the respiratory spectrum was measured with an edge operator. The DORK correction significantly reduced respiration-induced noise (image shift for EPI, blurring for spiral, ghosting for segmented acquisition). While spiral imaging was found to exhibit less noise than EPI before correction, the residual noise after the DORK correction was comparable. The correction is simple to apply and can correct for other sources of frequency drift and fluctuations in dynamic imaging.** Magn Reson Med 47:344–353, 2002. © 2002 Wiley-Liss, Inc.

**Key words:** respiration artifacts; physiological artifacts; global off-resonance; functional magnetic resonance imaging

In functional MRI (fMRI), a time-series of images is collected to monitor changes in the subject's physiology during a challenge, e.g., cognition, exercise, or contrast uptake. Invariably for such techniques, rapid acquisition such as echo-planar imaging (EPI) (1) or spiral imaging (2) is used in order to avoid loss of temporal information and to suppress artifacts from respiration and cardiac functions that are confounds to the challenge being monitored. In the case of blood oxygen level-dependant (BOLD) functional neuroimaging (3), which will be the primary focus of this work, an echo time (TE) comparable to  $T_2^*$  is used in order to maximize the sensitivity to small BOLD changes in  $T_2^*$ . Unfortunately, the relatively long TE also makes the acquisition sensitive to changes in resonance frequency and other factors, causing various artifacts.

NMR phase shifts can arise from instrument instability, bulk motion, or from cardiac and respiratory functions

(4–7). Phase variations between segments cause ghosting and extra noise in the time-series, which degrades functional data and the resulting maps. Zero-order phase (non-evolving in time) corrections using navigator echoes (8–10) or retrospective modeling of cardiac and respiratory modulations (11–13) have been employed to reduce these effects.

A major effect from respiration is that the resonance frequency in the brain region can vary in time even when the head of the subject is immobile (14–16). These first-order phase variations (evolving linearly in time) result from respiration-driven movement of organs in the thoracic and abdominal cavities, as well as to changes in the oxygenation state of the respired gas. The field modulations tend to vary weakly in the inferior–superior direction in accordance with relative proximity to the chest, although the dominant effect is a global frequency shift in the whole brain (16,17). In single-shot EPI images, changes in resonance frequency result in positional voxel shifts predominantly in the phase encode direction (15), while in spiral imaging the effect is to cause time-varying blurring, which in either case leads to increased time-series noise. In segmented acquisitions, frequency shifts also cause ghosting. For EPI imaging, the pixel shift in the *y* (phase encode) direction is  $\Delta y/p \approx \Delta f T_{\text{acq}}$ , where *p* is the pixel size,  $\Delta f$  is the frequency shift and  $T_{\text{acq}}$  is the duration of the *k*-space readout. For spiral imaging, sidelobes in the blurring point response function become prominent when  $r/p = 2 \Delta f T_{\text{acq}} > 1$ , where *r* is the radius (9). Geometric distortion corrections have been developed for static off-resonance conditions occurring because of local variations in magnetic susceptibility (18–20) and corrections have been made using navigator echo phase for magnetic field drift (5,21). However, to date no corrections have been reported for respiration-induced dynamic off-resonance effects.

In the present work we report a simple correction of “dynamic off-resonance in *k*-space” (DORK) that reduces the effects of time varying zero- and first-order phase shifts for EPI and spiral imaging. The correction assumes that variations in frequency and phase from respiration (or any other source of frequency drift or fluctuation) are uniform across the slice. The DORK correction uses phase information from a navigator echo as well as the imaging echo at the center of *k*-space to estimate the correction. The concept is an extension of that employed for mitigating effects of frequency drifts arising from an electric train (17), where only first-order corrections were required. It is expected that the effect of frequency variations increases with magnetic field strength and is inherently different for

\*Center for Magnetic Resonance Research, Department of Radiology, University of Minnesota Medical School, Minneapolis, Minnesota.

<sup>2</sup>Department of Radiology, Stanford University School of Medicine, Stanford, California.

Grant sponsor: National Institutes of Health; Grant numbers: RR08079; RR09784; RO1MH55346; Grant sponsors: W.M. Keck Foundation; National Foundation of Functional Brain Imaging (NFFBI).

\*Correspondence to: Josef Pfeuffer, Max-Planck Institute for Biological Cybernetics, Spemannstr. 38, 72076 Tübingen, Germany. E-mail: josef.pfeuffer@tuebingen.mpg.de

Received 14 June 2001; revised 10 September 2001; accepted 26 September 2001.

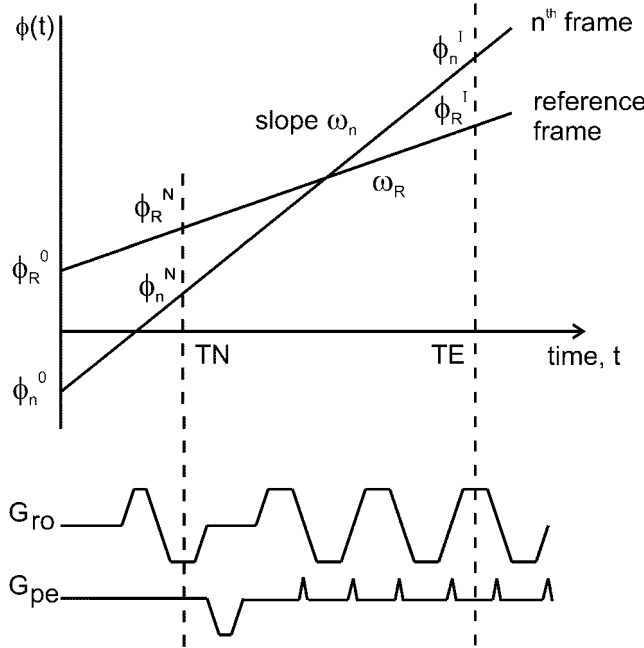


FIG. 1. Phase as a function of time during an EPI pulse sequence for two different time frames, the  $n$ th frame (index  $n$ ) and the reference frame (denoted with index  $R$ ). Experimental measurements of the phase are determined from a navigator signal at  $t = TN$  ( $\phi_n^N$  and  $\phi_R^N$ ) and from the center of the  $k$ -space at  $t = TE$  ( $\phi_n^I$  and  $\phi_R^I$ ). The phase intercepts at  $t = 0$  ( $\phi_n^0$  and  $\phi_R^0$ ) and corresponding slopes ( $\omega_n$  and  $\omega_R$ ) are determined for each image according Eq. [6] and used for the “dynamic off-resonance in  $k$ -space” (DORK) correction (Eq. [7]). For demonstration of experimental data, see Fig. 3.

EPI and spiral imaging. Therefore, we studied these effects on four volunteers at a magnetic field of 7 T and compared the results of corrections made for both EPI and spiral imaging.

## MATERIALS AND METHODS

### Theory

#### *Full Correction*

In accordance with the discussion above, the respiration is assumed to cause a global frequency shift due to modulation of the magnetic field at the site of the imaging slice, as well as a global phase shift of the NMR signal. With this model the phase of an isochromat accumulates linearly because of the off-resonance condition, and ideally two measurements at different evolution times are needed to calculate the initial phase  $\phi_o$  and frequency offset  $\omega$  (see Fig. 1). The phase is monitored by sampling the transverse magnetization with a nonphase-encoded navigator signal (a simple FID signal) at time  $TN$  and from the imaging echo signal at the center of  $k$ -space at time  $TE$ , both of which sample the signal integrated over the slice. The navigator signal can also be encoded in the readout direction as long as the signal at the center of the echo is chosen. In practice, the locations of the  $k$ -space origin for both the navigator and imaging echoes are found from the maximum signal modulus in a reference time frame and are kept fixed for all time frames in the time series under consideration.

Let us first consider single-shot dynamic imaging, in which many consecutive time frames are acquired. With reference to Fig. 1, for the  $n$ th time frame the phase  $\phi_n$  evolves as a function of time  $t$  due to a frequency shift  $\omega_n$  (in the absence of imaging gradients) and phase offset  $\phi_n^o$  at  $t = 0$  as:

$$\phi_n(t) = \phi_n^o + \omega_n t. \quad [1]$$

However, imaging gradients may cause eddy currents that result in additional phase accumulation. The phase of the navigator signal collected at time  $TN$  (superscript  $N$ ) is:

$$\phi_n^N = \phi_n^o + \omega_n TN + \phi^{Ng}, \quad [2]$$

where  $\phi^{Ng}$  represents the phase from eddy currents induced by gradients (possibly from a previous time frame in the case of a nonphase-encoded navigator). Similarly, the phase of the signal from the imaging acquisition at the center of  $k$ -space (superscript  $I$ ) at  $TE$  is:

$$\phi_n^I = \phi_n^o + \omega_n TE + \phi^{Ig}, \quad [3]$$

where  $\phi^{Ig}$  represents the phase from eddy currents induced by the imaging gradients. In the case of spiral trajectories,  $\phi^{Ig}$  may be small because the signal is sampled before the readout gradients begin, although some eddy current effects from previous time frames may be present. In the general case the last two terms in Eqs. [2] and [3] cannot be ignored and two measurements of phase ( $\phi_n^N$  and  $\phi_n^I$ ) are not sufficient to determine the unknowns. Therefore, a convenient solution is to use one of the time frames, say the  $R$ th one, as a reference to which all other frames are compared. Then phase differences between the current time frame and the reference frame do not contain the gradient term  $\phi^{Ig}$  and are computed to obtain the corrections to the phase and frequency of each time frame.

We have for the navigator phase difference:

$$\begin{aligned} \Delta\phi_n^N &\equiv (\phi_n^N - \phi_R^N) = (\phi_n^o - \phi_R^o) + (\omega_n - \omega_R)TN. \\ &\equiv \Delta\phi_n^o + \Delta\omega_n TN \end{aligned} \quad [4]$$

and similarly for the image phase difference:

$$\Delta\phi_n^I = \Delta\phi_n^o + \Delta\omega_n TE. \quad [5]$$

Eqs. [4] and [5] are then solved to obtain the changes of frequency  $\Delta\omega_n$  and phase  $\Delta\phi_n^o$ :

$$\begin{aligned} \Delta\omega_n &= (\Delta\phi_n^I - \Delta\phi_n^N)/(TE - TN) \\ \Delta\phi_n^o &= (TE\Delta\phi_n^N - TN\Delta\phi_n^I)/(TE - TN). \end{aligned} \quad [6]$$

Finally, for the  $k$ -space signal obtained during readout of the  $n$ th frame,  $S_n(t)$ , the corrected signal  $S_n'(t)$  is:

$$S_n'(t) = S_n(t)\exp[-i(\Delta\phi_n^o + \Delta\omega_n t)]. \quad [7]$$

The net result is that the corrected signal for all time frames will have a frame-independent residual error in phase and

frequency equal to that occurring during the reference acquisition, represented by the phase factor  $\exp[i(\phi_R^o + \omega_R^t)]$ . The resulting time series of images will therefore have constant residual artifacts. Since these artifacts do not vary, the time series will have reduced fluctuations.

In the case of multisegment imaging, each segment is treated independently, with its own reference maintained. If desired, the usual zeroth-order phase correction can be applied so that  $\phi_o$  is equalized across segments (8,9).

### Partial Correction

The full correction in Eq. [7] requires acquisition of a navigator signal from either an FID or a navigator echo. In some cases it may be desired to implement a correction without altering the pulse sequence, or to correct existing data collected without a navigator echo. In such cases, it is assumed that  $\Delta\phi_n^o$  does not vary with time frame  $n$  and any phase variations in  $\phi_n^l$  from frame to frame reflect only frequency shifts that are calculated as:

$$\Delta\omega_n = \Delta\phi_n^l / TE, \quad [8]$$

so that the correction to the imaging data in this case is:

$$S'_n(t) = S_n(t)\exp(-i\Delta\omega_n t). \quad [9]$$

### Data Acquisition

A total of four normal subjects (two female, two male) were enrolled for the study, which was approved by the institutional review board at the University of Minnesota. All subjects provided written consent. Both baseline control (continuous visual stimulation) and block visual stimulation scans were obtained for each subject. For stimulation of the full visual field, flashing LED goggles (Grass Instruments, Quincy, MA) were used. Continuous 10-Hz flicker was presented for baseline studies. A block paradigm with 28 s stimulus-on and 32 s stimulus-off (four epochs) was employed for functional activation studies.

MR imaging of the human visual cortex was performed on a 7 T / 90 cm horizontal bore magnet (Magnex Scientific, Abingdon, UK) interfaced to a Varian INOVA console (Varian, Palo Alto, CA). The system is equipped with a Magnex head gradient set, which is torque-balanced, self-shielded, and water-cooled (38 cm ID). Driven by a Siemens Harmony/Symphony 800V/300A gradient amplifier (Siemens, Erlangen, Germany), a maximum gradient strength of 40 mT/m was achieved with a rise rate of 200 mT/m/ms. For increased SNR, a quadrature 7-cm coil was used for RF transmit and receive at 300 MHz (22). Localized shimming was done using FAST(EST)MAP (23), providing a linewidth of 15–20 Hz in a 6-cm sphere, which covered most of the visual cortex.

Rapid imaging was performed with EPI and a spiral sequence in which the acquisition parameters were matched as closely as possible to make a comparison between both imaging schemes. Two sets of acquisition parameters were chosen: 1) one-segment (single-shot),  $64 \times 64$ -matrix, and 2) four-segment,  $128 \times 128$ -matrix (field-of-view 12.8 cm, slice thickness 6 mm, axial plane through the visual cortex, repetition time per segment 100 ms). The acquisition time for one

series was 4 min 20 s, which corresponded to a total of 2600 (single-shot) or 650 images (four-segment) per series.

### Echo Planar Imaging

A blipped EPI sequence was used for acquiring all EPI data. The sequence was implemented with a readout gradient waveform consisting of alternating trapezoidal lobes. Nonlinear sampling in time was used on the ramps of each gradient, providing equidistant sampling in the  $k$ -space along the readout direction. To minimize the Nyquist ghost, a reference scan was collected and used in conjunction with the algorithm of Bruder et al. (24) to correct for discrepancy between the odd and even echoes. This algorithm also reduced to a large extent the distortions caused by off-resonance, providing a reasonable registration between the EPI data and the anatomical scans.

In the single-shot case with 2-mm in-plane resolution, 64 phase-encode lines were acquired with a total readout duration of 45 ms. In the four-segment case with 1-mm in-plane resolution, 32 phase-encode lines were acquired in each segment with a readout duration of 42 ms per segment. The minimum echo time was 27 ms.

### Spiral Imaging

The spiral gradient design followed an analytical approach (25). For fine-tuning of the gradient performance, the  $k$ -space trajectory was measured on phantoms with self-encoding gradients (26). Gradient onset, gradient asymmetry,  $k$ -space center offset, and zero- and first-order gradients were adjusted for each set of parameters (27). The latter was necessary to compensate for imperfections in performance of the console/gradient system. The measured trajectory was used for reconstruction with  $k$ -space weighting and gridding following a commonly used approach (28). To check for the necessity of  $B_0$  inhomogeneity corrections, phase maps were calculated from images at multiple echo times. After localized shimming using second-order terms, additional inhomogeneity corrections in reconstruction were found to be unnecessary for image quality. In order to minimize reconstruction errors that might interfere with the noise characteristics, no off-resonance correction was used.

In the single-shot case with 2-mm in-plane resolution, a  $64 \times 64$ -matrix was acquired with a total readout duration of 28 ms (200 kHz sampling rate). In the four-segment case with 1-mm in-plane resolution, four spiral interleaves with 16 turns were acquired with a readout duration of 20 ms per interleave. The center of the spiral  $k$ -space (i.e., the nominal echo time) was set to 15 ms, corresponding to an effective echo time being slightly larger. Fat suppression or the use of spatial chemical-shift selective excitation pulses (29) was not found to be necessary due to shortened  $T_2^*$  at higher magnetic field strength.

### Data Analysis

The reconstructed EPI and spiral imaging series were analyzed with routines developed in PV-Wave (Visual Numerics, Boulder, CO) and MATLAB (MathWorks, Natick, MA). According to the introductory discussion, it was expected that the effects of off-resonance would be most prominent near the edges of image features. To demon-

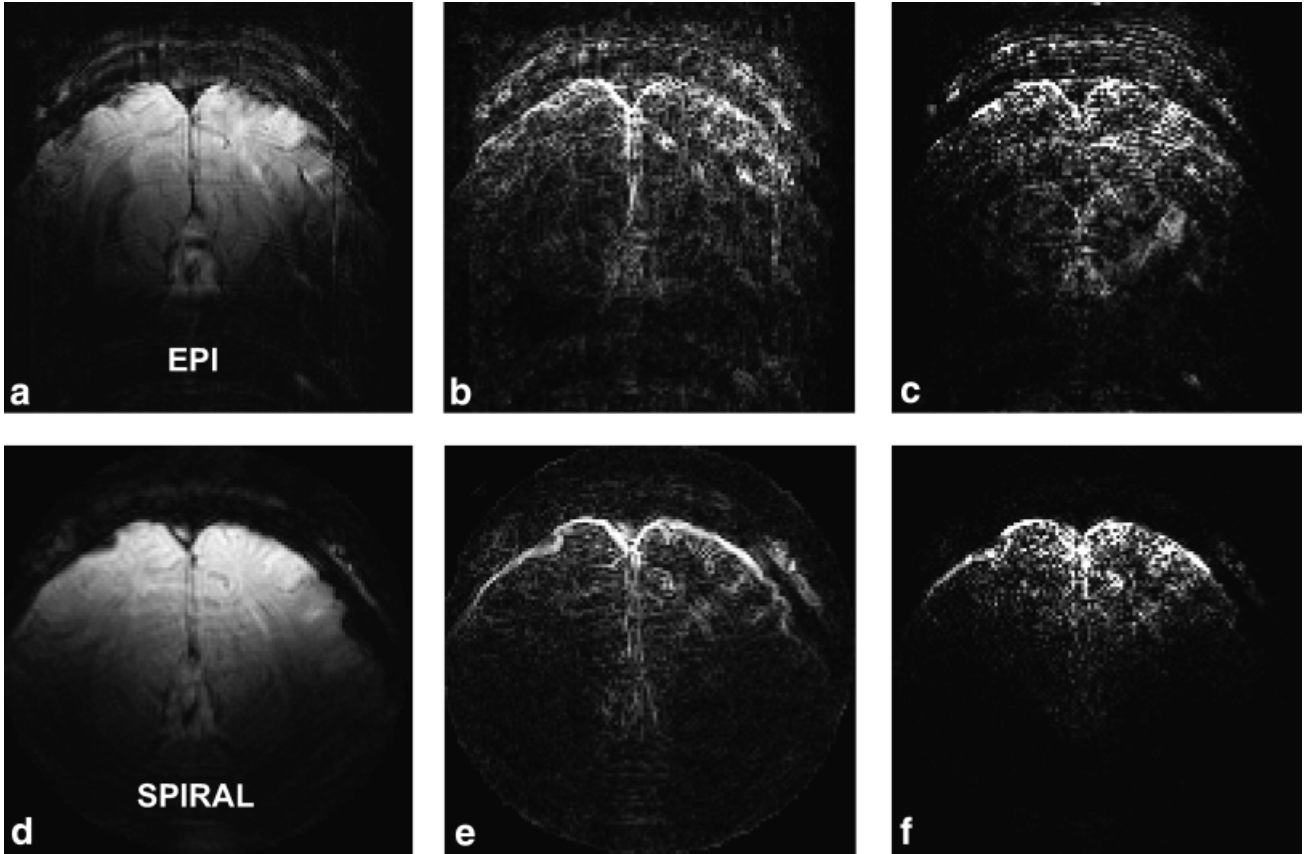


FIG. 2. To reveal structures in the  $T_2^*$ -weighted EPI (top) and spiral images (bottom), a grad-operator was applied to the images to create the  $\nabla$ -maps in **b**, **e**. Furthermore, difference maps before/after the DORK correction are depicted in **c**, **f**. When comparing these difference maps with the  $\nabla$ -maps, a good spatial correlation is found, which provides evidence that the  $\nabla$ -maps can be used for a threshold and user-independent metric. The complete metric is described in Data Analysis.

strate this, difference images were made of the EPI and spiral time series before and after the DORK correction (Fig. 2c,f). The difference images revealed that the correction is largest for image region where intensity changes are discernible, as near edges, fissures, and vessels. In the EPI case, image ghosts were also strongly influenced (Fig. 2c). These observations provided the rationale for generating the following objective metric to assess respiration-induced noise in either EPI or spiral time series images, which is independent of threshold and does not require a user-dependent region-of-interest.

To create the metric mask, an edge operator was applied to the images  $I_n$  in the time series, given by:

$$\nabla_n \equiv \sqrt{(\partial I_n / \partial x)^2 + (\partial I_n / \partial y)^2}, \quad [10]$$

where a three-point polynomial interpolation was used for the numerical derivative. By definition, this operator revealed the spatial changes in image intensity (Fig. 2b,e). As seen in Fig. 2, the  $\nabla$ -maps (Fig. 2b,e) compare well with the difference maps (Fig. 2c,f) for the EPI and spiral images. To generate a normalized mask reflecting voxels likely to be affected by respiration or other off-resonance conditions, the  $\nabla_n$ -maps were averaged for the whole time course, then multiplied with the average image intensity map, and squared and normalized as

$$\nabla \cdot \nabla = (\bar{I} \cdot \bar{\nabla})^2 / \sum_{\text{voxels}} (\bar{I} \cdot \bar{\nabla})^2. \quad [11]$$

This  $\nabla \cdot \nabla$ -mask function thereby provides a suitable weighting function that emphasizes the edge structures in the image without the need for thresholds or subjective intervention. With this  $\nabla \cdot \nabla$ -mask a characteristic time series and a power spectrum series were calculated.

#### Time Series Analysis

To create a typical time series reflecting the physiologically induced changes in the imaging series, for each image in the series a weighted average in the time domain was calculated using the metric  $\nabla \cdot \nabla$ -mask as weighting function. After detrending with a second-order polynomial, the normalized standard deviation (SD) of the time series  $\sigma_{\text{time}}$  and  $\sigma_{\text{time}}^{\text{corr}}$  before and after DORK correction was determined for all series and expressed as a percentage of the mean image intensity after detrending.

#### Time Series Analysis of Functional Data

To create characteristic time courses for the functional data sets, a weighted average in the time domain was calculated using the metric  $\nabla \cdot \nabla$ -mask multiplied with the

cross-correlation map as weighting function. The correlation map was generated using a boxcar reference function convolved with a standard hemodynamic response model.

#### Power Spectrum Analysis

To assess the fluctuations in selected spectral bands, a power spectrum analysis was used. It also has the advantage over the averaging in the time domain that the processing is insensitive to phase information. It is expected that the fluctuations in the time domain have different phase in different voxels and do not sum coherently. With EPI, for example, when the image shifts some voxels will exhibit signal increase while others will have decreased intensity. The spatial averaging in the time series analysis above would thereby underestimate the total variance.

The power spectrum analysis was performed for each voxel and a weighted average of the power spectra of all voxels was calculated using the metric  $\nabla \cdot \nabla$ -mask as weighting function. The normalized standard deviations  $\sigma_{\text{resp}}$ ,  $\sigma_{\text{card}}$ , and  $\sigma_{\text{total}}$  were then calculated for the spectral bands of the respiration ( $\sim 0.33 \pm 0.1$  Hz), the cardiac ( $\sim 1.0 \pm 0.1$  Hz), and for the total spectrum. These values were compared for the uncorrected and the DORK-corrected image series and were expressed as a percentage of the mean image intensity after detrending.

To compare across different runs and studies, the global frequency shift  $\Delta\omega$  was determined according Eq. [6] and its standard deviation  $\sigma_{\Delta\omega}$  was calculated after detrending. For the interstudy mean and standard error (SE),  $\sigma_{\text{resp}}$  and  $\sigma_{\text{total}}$  were then normalized by  $\sigma_{\Delta\omega}$ .

## RESULTS

In the measured time series at 7 T, respiration was a dominant source of physiologically induced fluctuations, which has been demonstrated recently (16). When comparing the respiratory recording using a pneumatic belt around the abdomen (Fig. 3a) to the MR-recorded image phase evolutions  $\phi^I(t)$  (Fig. 3b), a strong correlation was found with a cross-correlation coefficient of 0.84. The MR phase changes  $\phi^I(t)$  and  $\phi^N(t)$  followed the breathing of the subject in frequency, phase, and amplitude.

To calculate the dynamic off-resonance, two phase measurements at time TE and TN were used (Fig. 3b,c), taken from the center of the image  $k$ -space and from a separate navigator signal. According to Eq. [6], zero phase and

frequency evolutions  $\Delta\phi_n^o$  and  $\Delta\omega_n$  were deduced (Fig. 3d,e). The magnitude spectrum of the frequency evolution  $F\{\Delta\omega_n\}$  in Fig. 3f shows dominant spectral intensities around 0.33 Hz, which are attributed to respiratory-induced fluctuations. In addition, increased spectral compo-

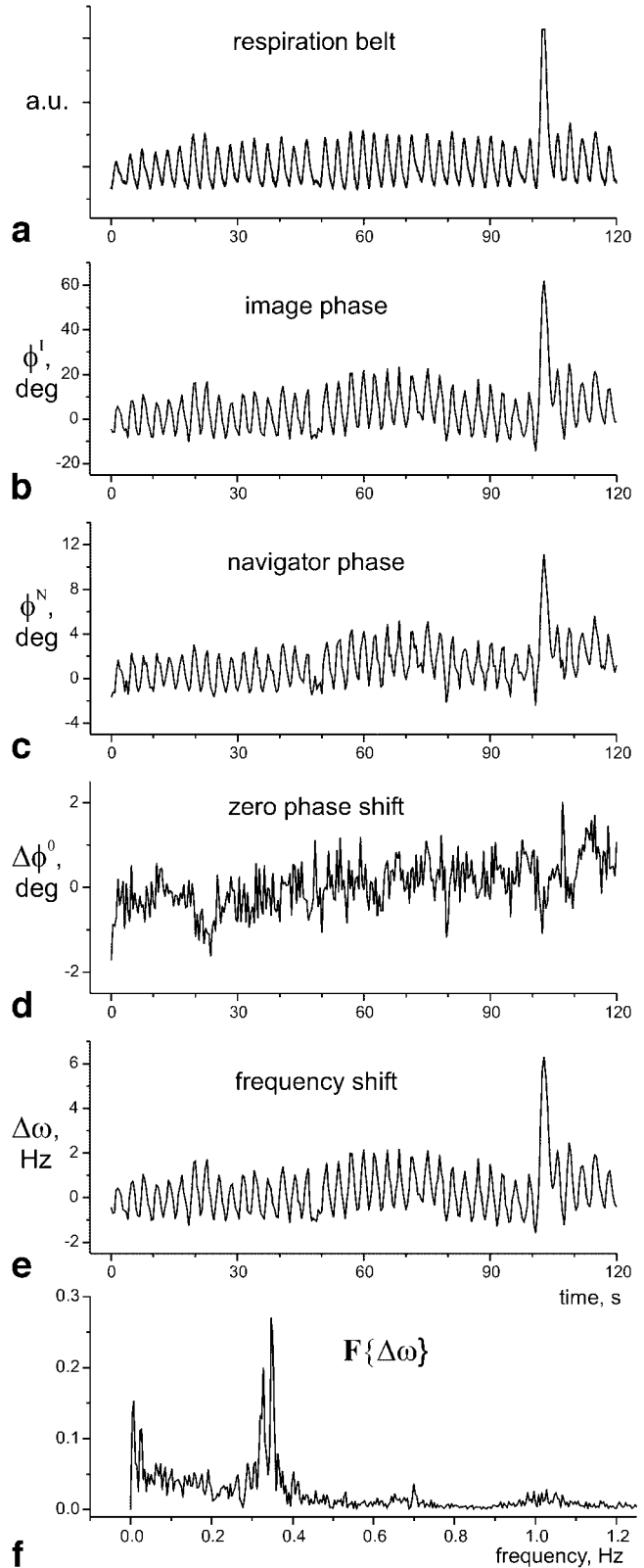


FIG. 3. Time courses from the pneumatic respiration belt (a) and the phase signals  $\phi^I(t)$ ,  $\phi^N(t)$  (b,c) acquired at the time of the center of the image  $k$ -space, TE, and at the time of the additional navigator echo, TN, respectively. The phase changes recorded by NMR closely follow the breathing of the subject in frequency, phase, and amplitude when compared to the respiratory recording. Zero phase shift,  $\Delta\phi^o$  and frequency shift,  $\Delta\omega$  (d,e) were calculated from the navigator phases  $\phi^N(t)$ ,  $\phi^I(t)$  according to Eq. [6] and subsequently used to correct the dynamic off-resonance in  $k$ -space (DORK) according to Eq. [7]. The magnitude spectrum of the frequency shift  $F\{\Delta\omega\}$  in f shows dominant frequency bands around 0.33 Hz and 1 Hz that are attributed to physiological fluctuations of respiratory and cardiac origin, respectively.

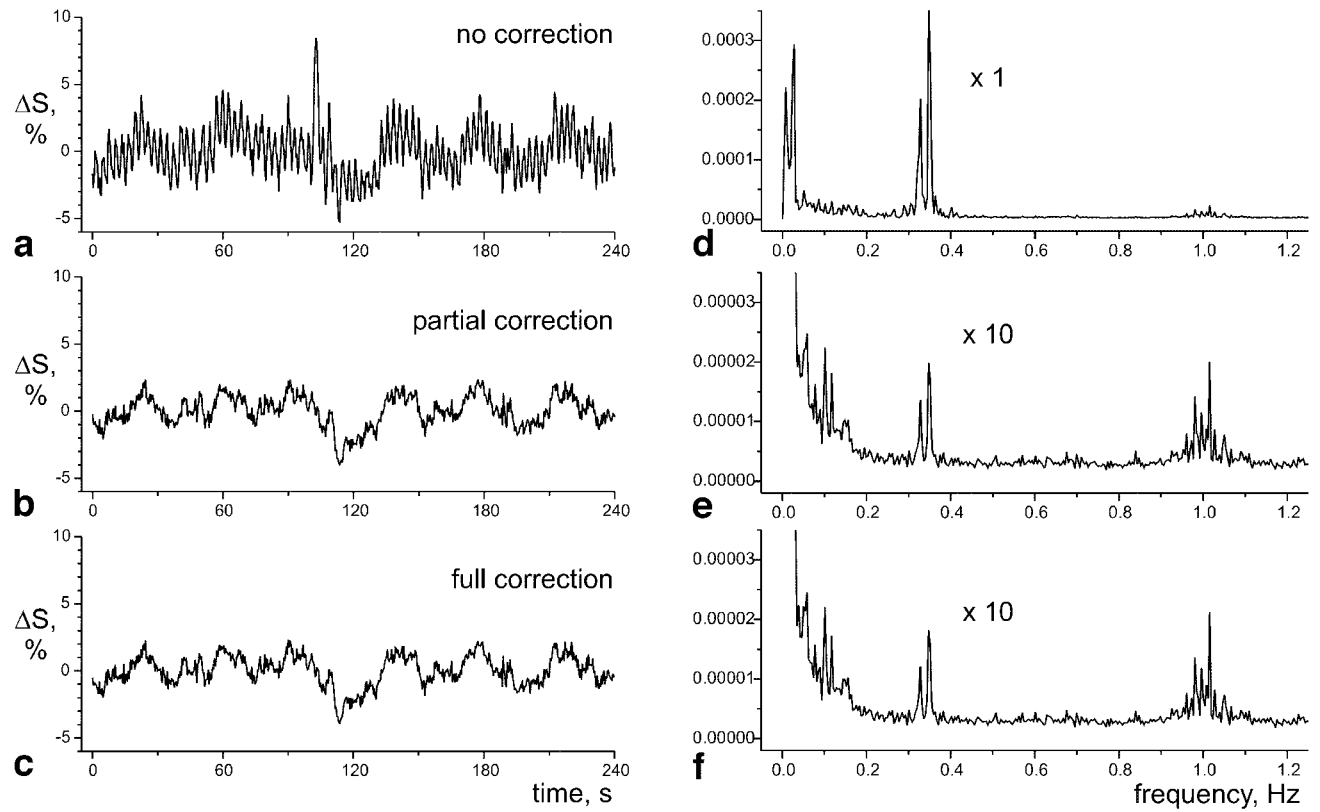


FIG. 4. Time courses and power spectra of a baseline study demonstrating the effect of the DORK correction on physiologically induced fluctuations. Using the partial correction (b,e), the fluctuations were decreased dramatically and were improved when applying the full DORK correction (c,f). The partial DORK correction uses only a single navigator phase (Eq. [9]), whereas the full zero- and first-order correction uses two navigator phases (Eq. [7]). In a-c the voxel-averaged time courses are shown with no, with partial, and with full correction. Corresponding SDs of the time series  $\sigma_{\text{time}}$  were 1.85%, 1.14%, and 1.11%, respectively. Similarly, in d-f the voxel-averaged power spectra are shown with no, with partial, and with full correction. Corresponding SDs  $\sigma_{\text{resp}}$  of the respiratory band ( $0.33 \pm 0.1$  Hz) were 1.89%, 0.43%, and 0.41%, and the relative spectral energy of the respiration band decreased from 56% to 13% and 12%, respectively.

nents at 1 Hz show fluctuations of cardiac origin. Remarkably, the frequency evolution  $\Delta\omega_n$  is highly correlated to the image phase evolutions  $\phi^I(t)$ , which is consistent with the zero phase shift  $\Delta\phi_n^o$  being very small (SD = 0.6 deg).

The effect of the DORK correction is demonstrated in Fig. 4 for EPI data (Subject 1). The time series analysis with the metric  $\nabla \cdot \nabla$ -mask showed significant reduction of fluctuations comparing the time course before correction (Fig. 4a) with the time course after the partial and the full DORK correction (one and two phase signals, Fig. 4b,c). The corresponding SDs of the time series  $\sigma_{\text{time}}$  decreased from 1.85% to 1.14% and 1.11%, respectively. The power spectrum analysis (Fig. 4d-f) provided similar results, but proved to exhibit higher fluctuations than the time series analysis because the latter underestimated the phase-incoherent noise. Spectral intensities, especially in the respiratory band ( $\sim 0.33 \pm 0.1$  Hz), decreased with the partial and the full DORK correction. The SDs  $\sigma_{\text{resp}}$  of the respiratory band decreased from 1.89% to 0.43% and 0.41%, and the corresponding relative spectral energy of respiration decreased from 56% to 13% and 12%. In the time series analysis, the phase of the fluctuations was incoherently averaged and diluted across voxels, which was not the case in the power spectrum analysis, where the spatial averaging was performed after the power spectrum calcu-

lation. The total SD  $\sigma_{\text{total}}$  of 3.4% was therefore larger than calculated from the time series ( $\sigma_{\text{time}} = 1.9\%$ ).

Detailed results acquired from Subject 1 in a single session are summarized in Table 1, which lists single-shot and four-segment data from EPI and spiral imaging. Normalized SDs are shown before and after the DORK correction using continuous ("control") and blockwise ("stim") visual stimulation. When comparing the SD before and after DORK correction, in all cases a significant improvement of  $\sigma_{\text{time}}$ ,  $\sigma_{\text{total}}$ , and  $\sigma_{\text{resp}}$  is discernible;  $\sigma_{\text{card}}$ , however, was not significantly changed. This points to the fact that the source of the dynamic off-resonance is mainly induced by respiration on a global level, i.e., across the entire image FOV.

When Subject 1 was asked to breathe deeply throughout several scans, the SD of the global frequency shift  $\sigma_{\Delta\omega}$  increased from the normal range of 0.7–0.9 Hz to 2.8–3.5 Hz, a more than threefold increase. This demonstrates that, in addition to the geometry of the subject's breathing apparatus, the breathing habits also play an important role. A single deep breath could change the dynamic off-resonance fluctuation from 2 Hz to 8 Hz peak-to-peak (Fig. 3e). With an increased  $\sigma_{\Delta\omega}$  caused by deeper breathing,  $\sigma_{\text{total}}$ ,  $\sigma_{\text{resp}}$ , and  $\sigma_{\text{time}}$  were increased, whereas  $\sigma_{\text{card}}$  was similar (Table 1).

Table 1

Normalized SDs of the Global Off-Resonance, the Time Series, and Power Spectra Bands Acquired From Subject 1

EPI	Single-shot		Four-segment			
	Control <sup>d</sup>	Stim	Control	Stim	Deep	Deep
$\sigma_{\Delta\omega}$ , Hz <sup>a</sup>	0.75	0.90	0.85	0.71	2.8	3.0
$\sigma_{\text{time}}$ , % <sup>b</sup>	1.2	1.7	1.9	1.8	6.3	4.9
$\sigma_{\text{time}}^{\text{corr}}$ , %	0.53	1.2	1.1	1.2	1.8	1.7
$\sigma_{\text{total}}$ , % <sup>c</sup>	2.6	3.2	3.4	3.4	9.7	8.3
$\sigma_{\text{total}}^{\text{corr}}$ , %	1.5	2.3	2.5	2.6	3.4	4.2
$\sigma_{\text{card}}$ , %	0.40	0.48	0.54	0.65	0.47	0.60
$\sigma_{\text{card}}^{\text{corr}}$ , %	0.36	0.52	0.54	0.64	0.40	0.51
$\sigma_{\text{resp}}$ , %	1.9	1.8	1.9	1.8	9.4	7.5
$\sigma_{\text{resp}}^{\text{corr}}$ , %	0.33	0.42	0.41	0.40	2.7	2.8
SPIRAL	Single-shot		Four-segment			
	Control	Stim	Control	Stim	Deep	Deep
$\sigma_{\Delta\omega}$ , Hz	0.80	0.76	0.76	0.70	3.4	3.5
$\sigma_{\text{time}}$ , %	0.85	1.1	0.85	1.2	1.5	1.4
$\sigma_{\text{time}}^{\text{corr}}$ , %	0.50	0.85	0.83	1.2	1.4	0.96
$\sigma_{\text{total}}$ , %	1.9	2.1	2.4	2.5	3.8	3.5
$\sigma_{\text{total}}^{\text{corr}}$ , %	1.2	1.6	2.2	2.4	2.9	2.4
$\sigma_{\text{card}}$ , %	0.25	0.39	0.52	0.66	0.10	0.13
$\sigma_{\text{card}}^{\text{corr}}$ , %	0.27	0.41	0.53	0.66	0.10	0.12
$\sigma_{\text{resp}}$ , %	1.4	1.2	0.76	0.49	3.3	3.1
$\sigma_{\text{resp}}^{\text{corr}}$ , %	0.31	0.26	0.38	0.29	2.1	1.8

<sup>a</sup> $\sigma_{\Delta\omega}$ : SD of the global frequency shift  $\Delta\omega$  calculated by Eq. [6].<sup>b</sup> $\sigma_{\text{time}}$ : SD calculated by time series analysis before and after the DORK correction. Weighted averaging metric was based on a  $\nabla \cdot \nabla$ -mask (see Data Analysis).<sup>c</sup> $\sigma_{\text{total}}$ ,  $\sigma_{\text{card}}$ ,  $\sigma_{\text{resp}}$ : SDs of the image series calculated by power spectrum analysis before and after the DORK correction. Depicted are the SDs based on the total spectrum, the respiration band ( $\sim 0.33 \pm 0.1$  Hz), and the cardiac band ( $\sim 1.0 \pm 0.1$  Hz).<sup>d</sup>Data were acquired with continuous visual stimulation (control) and with blockwise stimulus-on/stimulus-off (stim). For two runs the subject was asked to breath deeper than usual (deep).

Data from all studies are summarized in Table 2:  $\sigma_{\Delta\omega}$ ,  $\sigma_{\text{total}}$ ,  $\sigma_{\text{resp}}$ , and  $\sigma_{\text{resp}}^{\text{corr}}$  for the series of EPI and spiral imaging. With the DORK correction, the SD of the respiration and thereby the total SD of fluctuations were significantly improved in all series:  $P < 10^{-5}$  for single-shot, and  $P < 10^{-4}$  (EPI),  $P < 2 \cdot 10^{-3}$  (SPIRAL) for four-segment (paired  $t$ -test  $\sigma_{\text{resp}}$  vs.  $\sigma_{\text{resp}}^{\text{corr}}$ ). Cardiac noise was not improved:  $P > 0.2$  (paired  $t$ -test  $\sigma_{\text{card}}$  vs.  $\sigma_{\text{card}}^{\text{corr}}$ ). Before correction, spiral imaging showed less fluctuation than EPI:  $P < 2 \cdot 10^{-5}$  for single-shot and  $P < 2 \cdot 10^{-4}$  for four-segment (paired  $t$ -test  $\sigma_{\text{total}}^{\text{EPI}}$  vs.  $\sigma_{\text{total}}^{\text{SPIRAL}}$ ). However, after the DORK correction both EPI and spiral imaging had similar residual noise:  $P > 0.02$  for single-shot and  $P > 0.3$  for four-segment (paired  $t$ -test  $\sigma_{\text{resp}}^{\text{corr, EPI}}$  vs.  $\sigma_{\text{resp}}^{\text{corr, SPIRAL}}$ ). Therefore, the correction of the global dynamic off-resonance fluctuations reduced significantly for both EPI and spiral imaging.

To demonstrate utility of the DORK correction in functional imaging, high-resolution ( $1 \times 1 \text{ mm}^2$ ) functional activation maps were derived for Subject 1 (Study 1-2) with a four-segmented acquisition (Fig. 5). The EPI (Fig. 5a) and spiral imaging (Fig. 5b) activation maps were similar. An increased number of activated voxels (colored in blue) was found after the DORK correction. At a cross-correlation threshold larger than 0.2, 91 additional voxels out of 809 were found for EPI (+11%) and 44 additional voxels out of 870 were found for spiral (+5%). A substantial reduction in the noise was demonstrated in the time courses after correction for both EPI (Fig. 6a,b) and spiral imaging (Fig. 6c,d).

## DISCUSSION

In the present work, a simple correction of physiologically induced global off-resonance was developed. In addition, the first functional spiral imaging data of human brain at 7 T was presented. EPI and spiral imaging, single-shot and four-segment, were used to assess the noise characteristic of dynamic image series of the human brain. The measurements were obtained at very high magnetic field, where respiration-induced effects are expected to be large and more significant than at lower fields (11). The results demonstrated that 1) the DORK correction reduced noise significantly for both imaging trajectories, spiral and EPI; 2) spiral imaging was found to exhibit less noise than EPI before correction; and 3) after the DORK correction both EPI and spiral imaging exhibited a similar residual noise.

The DORK correction assumes that frequency offsets are constant across the imaging slice, so that phase information can be obtained from the center of  $k$ -space and from an additional navigator signal. It is an extension of the method employed for mitigating effects of frequency drifts arising from an electric train (17), where only first-order corrections were used. In addition to changes of frequency  $\Delta\omega_n$ , the method also assesses and corrects changes of the zero-order phase  $\Delta\phi_n^o$ . Because the major source of *global* physiological effects on frequency is the respiration, the DORK correction affected noise mainly in the respiration band. Cardiac noise was not significantly reduced by the DORK correction because these artifacts do not arise from global frequency shifts,

Table 2  
Normalized SDs of Global Frequency Shift and Different Power Spectrum Bands ( $\Gamma$ , Total and Respiration)

Study	Single-shot			Spiral			Four-segment			Spiral		
	FREQ $\sigma_{\Delta\omega}$ , Hz	FREQ $\sigma_{\text{total}}$ , %	EPI $\sigma_{\text{resp}}$ , %	FREQ $\sigma_{\Delta\omega}$ , Hz	FREQ $\sigma_{\text{total}}$ , %	EPI $\sigma_{\text{resp}}$ , %	FREQ $\sigma_{\Delta\omega}$ , Hz	FREQ $\sigma_{\text{total}}$ , %	EPI $\sigma_{\text{resp}}$ , %	FREQ $\sigma_{\Delta\omega}$ , Hz	FREQ $\sigma_{\text{total}}$ , %	EPI $\sigma_{\text{resp}}$ , %
1-1 control	0.78	2.6	1.9	0.33	1.9	1.4	0.31	0.81	3.4	1.9	0.41	2.4
1-2 stim	0.83	3.2	1.8	0.42	2.1	1.2	0.26	0.71	3.4	1.8	0.40	2.5
1-3 deep												
1-4 deep												
2-1 control	1.0	3.2	2.2	0.51	3.0	1.9	0.70	1.1	4.3	2.0	1.3	3.7
2-2 stim	1.0	2.9	1.9	0.38	2.4	1.8	0.39	1.1	4.3	1.9	1.7	3.4
2-3 control	1.0	3.0	2.1	0.41	2.4	1.5	0.31	1.1	3.5	1.9	0.69	2.6
3-1 control	1.3	3.9	2.8	1.0	2.8	2.2	1.0	1.3	4.3	2.7	1.7	3.7
3-2 stim	1.2	4.5	2.9	1.7	2.8	2.0	1.1	1.2	4.3	2.7	1.4	3.6
3-3 control												
4-1 control	1.5	3.9	2.6	1.0	3.2	1.8	0.83	1.6	4.4	2.8	1.5	3.7
4-2 stim	1.6	3.6	2.4	1.1	3.3	1.9	0.91	1.6	4.7	2.3	1.3	4.0
4-3 control												
Mean $\pm$ SE	1.0	$3.24 \pm 0.15$	$2.17 \pm 0.11$	$0.71 \pm 0.12$	$2.27 \pm 0.09$	$1.49 \pm 0.08$	$0.52 \pm 0.07$	1.0	$3.44 \pm 0.17$	$2.08 \pm 0.15$	$0.97 \pm 0.09$	$2.52 \pm 0.21$

$\sigma_{\Delta\omega}$ ,  $\sigma_{\text{total}}$ ,  $\sigma_{\text{resp}}$  and  $\sigma^{\text{corr}}$  were calculated as in Table 1.

Interstudy mean and SE of  $\sigma$  were determined after normalization with the corresponding  $\sigma_{\Delta\omega}$ .

but are more local in nature, e.g., cardiac pulsation in CSF and areas close to large blood vessels. Since the metric was tailored to detect changes of edges, the contribution of cardiac noise  $\sigma_{\text{card}}$  is certainly underestimated in Table 1. Quantification of  $\sigma_{\text{card}}$  was not the point of this study and is only reported for completeness.

The partial correction, which does not require a navigator signal other than the  $k = 0$  data and therefore can be implemented with no change to existing pulse sequences, performed nearly as well as the full correction (Fig. 4). Using the full correction, the fluctuations of the zero phase were found to be small, which correlates with the good performance observed when using only the image phase signal in the partial correction. Zeroth-order phase shifts may arise from bulk motion of the head or other motions induced by physiological functions. We have found that with suitable restraint of the head and/or the use of a bite bar, these fluctuations are generally small. Gradient moment compensation in the slice direction (not used here) may also be beneficial. The full correction, however, provides a further practical advantage: it is more robust and less sensitive to the exact value of the sequence timing TE, since only the difference time (TE–TN) is needed to calculate the frequency shift.

A key feature of the correction is its minimal computational effort and its robustness against low SNR, because the phase is calculated from the signal integral over the whole image. Therefore, it is recommended to be a part of routine EPI and spiral image reconstruction. For most applications, particularly at higher magnetic field, the dominant effects of physiologically induced noise are reduced.

Previously published retrospective corrections in  $k$ -space and image-space, e.g., PhysioFix (11) and RETROICOR (12,13), can be used alternatively or in addition to correct for local sources of noise like cardiac fluctuations. A preliminary comparison of PhysioFix and the DORK correction indicated that PhysioFix did not correct respiratory noise as well as the DORK correction, but improved on the cardiac noise. For example,  $\sigma_{\text{resp}}$  of Study 1-1 was decreased from 1.89% to 0.82% with PhysioFix and 0.41% with DORK;  $\sigma_{\text{card}}$  was decreased from 0.54% to 0.32% with PhysioFix, but was unaltered with DORK. While PhysioFix is less restrictive in its assumptions about the nature of the noise, it relies on good S/N and in practice may not work as well for respiration. In addition, in its present implementation, cycle-to-cycle amplitude changes in respiration were not accounted for. It has been shown recently that respiration-induced  $B_0$  fluctuations are spatially distributed and increase along the Z-axis towards the lungs (16). Supported by these experimental results, it can be well assumed that, in the current axial imaging plane, the frequency offset is approximately spatially uniform. Vice versa, from the fact that the DORK correction performed very well, it can be concluded that most of the frequency shift is well characterized by a global frequency average. The DORK correction may not work as well for sagittal and coronal images when the off-resonance is more spatially varying. For these cases, the method can be easily extended to incorporate a spatial dependence, e.g., by using navigators after the readout as well as before or by utilizing phase information of the voxels in the image domain. For cardiac noise, the noise is not appropriately described by a global off-resonance shift, and therefore the DORK algorithm provided no significant correction. In this

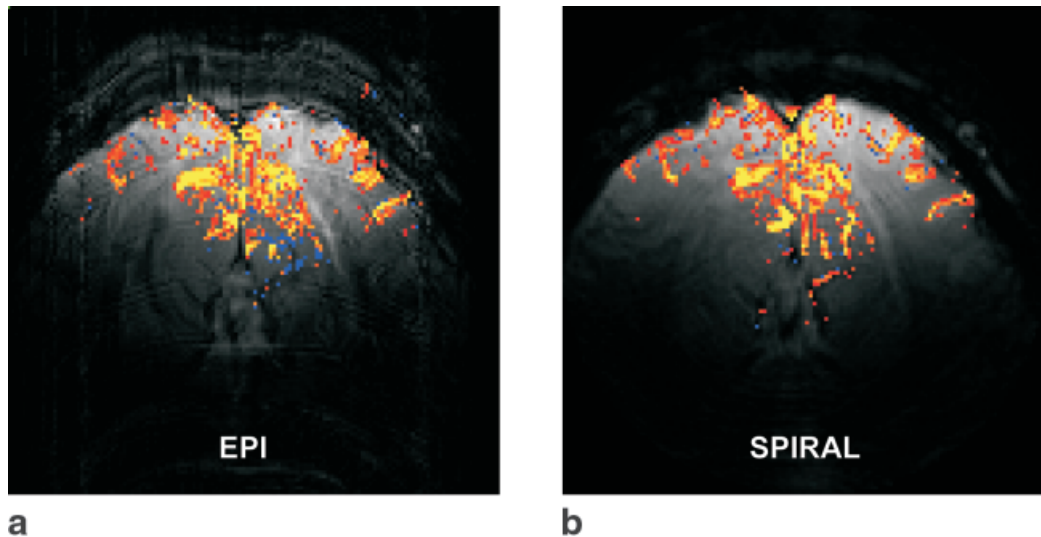


FIG. 5. Functional BOLD activation maps acquired by EPI (a) and spiral imaging (b) with four-segments and 1-mm spatial resolution. Cross-correlation coefficients range from 0.2 (red) to  $\geq 0.4$  (yellow). With the DORK correction, the number of activated voxels increased by 11% (EPI) and 5% (spiral). Additional voxels after correction are colored blue.

case, a correction with a retrospective technique in image-space is expected to perform better.

During deep breathing, in addition to the phase and frequency noise, severe changes in the amplitude correlated with respiration were observed that remained uncorrected (not shown). As described previously (11), a possible source of this amplitude change might have been physical through-plane motion of the slice induced by breathing. In event-related fMRI experiments the amplitude changes caused by respiration could be mistaken for functional activation and vice versa. Since the DORK correction only changes phase and frequency information,

amplitude fluctuations are not corrected. It was found that at high magnetic field, proper training of the volunteers can appreciably reduce the respiration fluctuations by prompting them to breath relatively shallowly and by avoiding single, occasionally deep breaths during the study. This is supported by the data shown in Table 1, where the SD of the frequency change in the same subject increased more than threefold with deep breathing.

In multisegment and multislice imaging the effect of respiration-induced fluctuation and thereby image artifacts is often the most prominent, as shown in the tables. For multisegment EPI, severe segmentation artifacts and

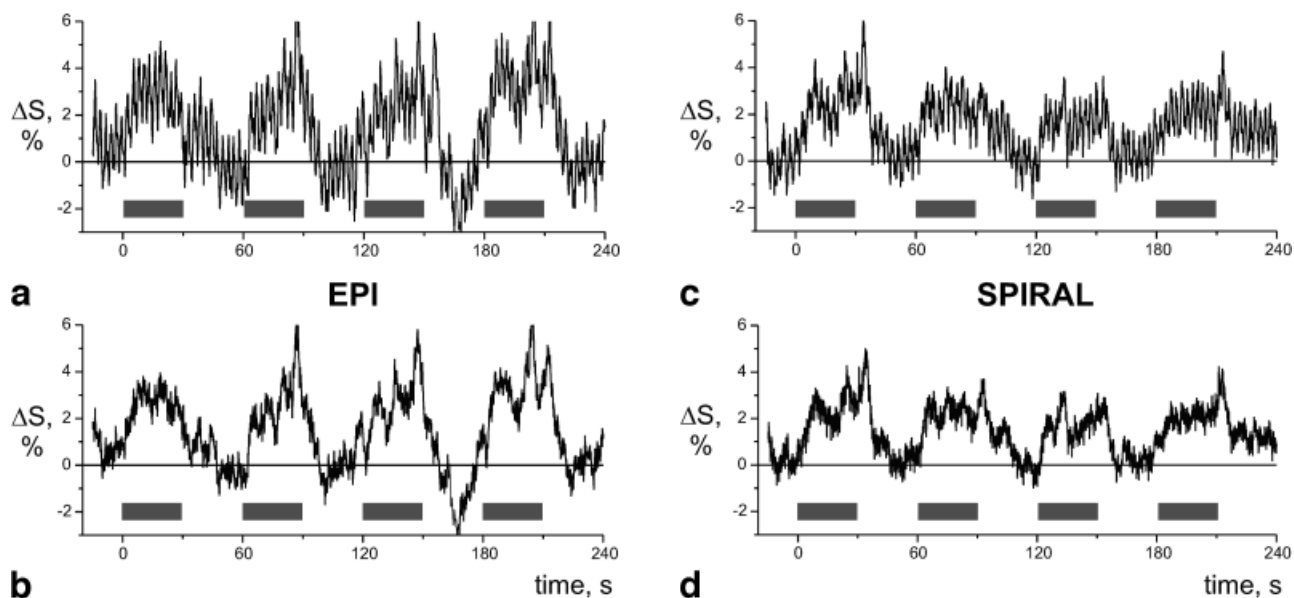


FIG. 6. Time courses of a functional BOLD study demonstrating the effect of the DORK correction on physiologically induced fluctuations. Relative signal fluctuations are shown before and after the DORK correction for EPI (a,b) and spiral imaging (c,d), which demonstrate a significant noise decrease after correction. To create the characteristic time courses for the functional datasets, an average was calculated using the cross-correlation map multiplied with the metric  $\nabla \cdot \nabla$ -mask as weighting function.

ghosting is expected, which can be significantly improved by applying the DORK correction. It was noticed that, in the multisegment case, the total noise upon a large dynamic off-resonance (deep breathing) was much larger for EPI ( $\sigma_{\text{total}} = 8\text{--}10\%$ ) than for spiral imaging ( $\sigma_{\text{total}} = 4\%$ ).

The difference in the noise characteristics between EPI and spiral imaging is caused by the fact that frequency variations have different effects on the EPI and spiral images. Whereas off-resonance causes voxel displacement, distortion, and misregistration in EPI images, it results in blurring and decreased effective image resolution, but leaves the registration intact in spiral images. Using the metric based on identifying voxels near edges with a mask operator, image blurring in the spiral case is less noisy than a linear voxel displacement in the case of EPI. In addition, a segmented spiral acquisition benefits from a *redundant* oversampling at the *k*-space origin and from its insensitivity to motion due to compensated gradient moments (12). Spiral imaging also allows a much shorter minimum echo time and *k*-space can be more efficiently sampled, which reduces the total acquisition time and sensitivity to off-resonance effects. Although both image acquisition schemes show different effects upon off-resonance, they consistently exhibit a similar residual noise after the correction is applied.

Application of the DORK correction is not limited to respiration-induced fluctuations, as it can be used for correction of any other source of global frequency change in a dynamic imaging series, such as magnetic field drift. This may be very significant for some scanners, which exhibit field drifts due to heating of the passive or resistive shims (30) or the gradient coils from extended periods of rapid imaging common in fMRI.

In summary, the significance of the DORK correction lies in its efficiency and simplicity and its usefulness for many kinds of time-series imaging studies. Functional imaging and other difference and phase imaging techniques, e.g., arterial spin labeling for blood flow measurements, can benefit greatly from its use. The DORK correction significantly reduces the noise in single-shot imaging and reduces ghosting and segmentation artifacts in multisegmented imaging. Finally, although not quantified rigorously, the partial correction provides most of the benefits of the full correction and requires no change to the pulse sequence.

## ACKNOWLEDGMENTS

The authors thank Shantanu Sarkar for help with the spiral reconstruction, John Strupp for help with the EPI reconstruction, and Gregor Adriany, Peter Andersen, and Hellmut Merkle for hardware support of the 7T system. J.P. thanks Ann-Katrin Marie for keeping him smiling every day. G.H.G. performed this work as a guest at the CMRR, for which he gratefully acknowledges the support of Prof. Ugurbil and other members of the Center.

## REFERENCES

- Mansfield P. Multi-planar image formation using NMR spin echoes. *J Phys Chem C* 1977;10:L55–L58.
- Noll DC, Cohen JD, Meyer CH, Schneider W. Spiral *k*-space MR imaging of cortical activation. *J Magn Reson Imag* 1995;5:49–56.
- Ogawa S, Lee TM, Kay AR, Tank DW. Brain magnetic resonance imaging with contrast dependent on blood oxygenation. *Proc Natl Acad Sci USA* 1990;87:9868–9872.
- Poncelet BP, Wedeen VJ, Weisskoff RM, Cohen MS. Brain parenchyma motion: measurement with cine echo-planar MR imaging. *Radiology* 1992;185:645–651.
- Wowl B, McIntyre MC, Saunders JK. *k*-Space detection and correction of physiological artifacts in fMRI. *Magn Reson Med* 1997;38:1029–1034.
- Frank LR, Buxton RB, Wong EC. Estimation of respiration-induced noise fluctuations from undersampled multislice fMRI data. *Magn Reson Med* 2001;45:635–644.
- Le TH, Hu X. Retrospective estimation and correction of physiological artifacts in fMRI by direct extraction of physiological activity from MR data. *Magn Reson Med* 1996;35:290–298.
- Hu X, Kim SG. Reduction of signal fluctuation in functional MRI using navigator echoes. *Magn Reson Med* 1994;31:495–503.
- Glover GH, Lai S. Self-navigated spiral fMRI: interleaved versus single-shot. *Magn Reson Med* 1998;39:361–368.
- Noll DC, Genovese CR, Vazquez AL, O'Brien JL, Eddy WF. Evaluation of respiratory artifact correction techniques in multishot spiral functional MRI using receiver operator characteristic analyses. *Magn Reson Med* 1998;40:633–639.
- Hu X, Le TH, Parrish T, Erhard P. Retrospective estimation and correction of physiological fluctuation in functional MRI. *Magn Reson Med* 1995;34:201–212.
- Glover GH, Li TQ, Ress D. Image-based method for retrospective correction of physiological motion effects in fMRI: RETROICOR. *Magn Reson Med* 2000;44:162–167.
- Chuang KH, Chen JH. IMPACT: Image-based physiological artifacts estimation and correction technique for functional MRI. *Magn Reson Med* 2001;46:344–353.
- Noll DC, Schneider W. Theory, simulation and compensation of physiological motion artifacts in functional MRI. In: IEEE Int Conf Image Process, Austin, 1994. p 40–44.
- Raj D, Paley DP, Anderson AW, Kennan RP, Gore JC. A model for susceptibility artefacts from respiration in functional echo-planar magnetic resonance imaging. *Phys Med Biol* 2000;45:3809–3820.
- van de Moortele P-F, Pfeuffer J, Glover GH, Ugurbil K, Hu X. Respiration-induced  $B_0$  fluctuations in the human brain at 7 Tesla and its spatial distribution. *Magn Reson Med* 2002, in press.
- Durand E, Van De Moortele PF, Pachot-Clouard M, Le Bihan D. Artifact due to  $B_0$  fluctuations in fMRI: correction using the *k*-space central line. *Magn Reson Med* 2001;46:198–201.
- Noll DC, Pauly JM, Meyer CH, Nishimura DG, Macovski A. Deblurring for non-2D Fourier transform magnetic resonance imaging. *Magn Reson Med* 1992;25:319–333.
- Jeppard P, Balaban RS. Correction for geometric distortion in echo planar images from  $B_0$  field variations. *Magn Reson Med* 1995;34:65–73.
- Irarrázabal P, Meyer CH, Nishimura DG, Macovski A. Inhomogeneity correction using an estimated linear field map. *Magn Reson Med* 1996;35:278–282.
- Liu HL, Kochunov P, Lancaster JL, Fox PT, Gao JH. Comparison of navigator echo and centroid corrections of image displacement induced by static magnetic field drift on echo planar functional MRI. *J Magn Reson Imag* 2001;13:308–312.
- Adriany G, Pfeuffer J, Yacoub E, van de Moortele P-F, Shmuel A, Andersen P, Hu X, Vaughan JT, Ugurbil K. A half-volume transmit/receive coil combination for 7 Tesla applications. In: Proc 9th Scientific Meeting ISMRM, Glasgow, 2001. p 1097.
- Grueter R, Tkac I. Field mapping without reference scan using asymmetric echo-planar techniques. *Magn Reson Med* 2000;43:319–323.
- Bruder H, Fischer H, Reinfelder HE, Schmitt F. Image reconstruction for echo planar imaging with nonequidistant *k*-space sampling. *Magn Reson Med* 1992;23:311–323.
- Glover GH. Simple analytic spiral *k*-space algorithm. *Magn Reson Med* 1999;42:412–415.
- Takahashi A, Peters T. Compensation of multi-dimensional selective excitation pulses using measured *k*-space trajectories. *Magn Reson Med* 1995;34:446–456.
- Pfeuffer J, Sarkar S, van de Moortele P-F, Ugurbil K, Hu X. Spiral imaging on a human ultra-high-field scanner. In: Proc 9th Scientific Meeting ISMRM, Glasgow, 2001. p 1778.
- Jackson JI, Meyer CH, Nishimura DG, Macovski A. Selection of a convolution function for Fourier inversion using gridding. *IEEE Trans Med Imag* 1991;10:473–478.
- Meyer CH, Pauly JM, Macovski A, Nishimura DG. Simultaneous spatial and spectral selective excitation. *Magn Reson Med* 1990;15:287–304.
- Henry PG, Van De Moortele PF, Giacomini E, Nauerth A, Bloch G. Field-frequency locked *in vivo* proton MRS on a whole-body spectrometer. *Magn Reson Med* 1999;42:636–642.